



Temperature-dependent kinetic pathways featuring distinctive thermal-activation mechanisms in structural evolution of ice VII

HPSTAR
996-2020

Chuanlong Lin^a, Xuqiang Liu^a, Xue Yong^{b,c}, John S. Tse^{a,b,1}, Jesse S. Smith^d, Niall J. English^e, Bihan Wang^a, Mei Li^a, Wenge Yang^{a,1}, and Ho-Kwang Mao^a

^aCenter for High Pressure Science and Technology Advanced Research, 100094 Beijing, People's Republic of China; ^bDepartment of Physics and Engineering Physics, University of Saskatchewan, 57N 5E2 Saskatoon, Canada; ^cDepartment of Chemistry, University of Calgary, Calgary, AB T2N 4V8, Canada; ^dHigh Pressure Collaborative Access Team, X-ray Science Division, Argonne National Laboratory, Argonne, IL 60439; and ^eSchool of Chemical and Bioprocess Engineering, University College Dublin, Belfield, Dublin 4, Ireland

Edited by Michael L. Klein, Temple University, Philadelphia, PA, and approved May 28, 2020 (received for review April 25, 2020)

Ice amorphization, low- to high-density amorphous (LDA-HDA) transition, as well as (re)crystallization in ice, under compression have been studied extensively due to their fundamental importance in materials science and polymorphism. However, the nature of the multiple-step “reverse” transformation from metastable high-pressure ice to the stable crystalline form under reduced pressure is not well understood. Here, we characterize the rate and temperature dependence of the structural evolution from ice VII to ice I recovered at low pressure (~5 mTorr) using in situ time-resolved X-ray diffraction. Unlike previously reported ice VII (or ice VIII)→LDA→ice I transitions, we reveal three temperature-dependent successive transformations: conversion of ice VII into HDA, followed by HDA-to-LDA transition, and then crystallization of LDA into ice I. Significantly, the temperature-dependent characteristic times indicate distinctive thermal activation mechanisms above and below 110–115 K for both ice VIII-to-HDA and HDA-to-LDA transitions. Large-scale molecular-dynamics calculations show that the structural evolution from HDA to LDA is continuous and involves substantial movements of the water molecules at the nanoscale. The results provide a perspective on the interrelationship of polymorphism and unravel its underpinning complexities in shaping ice-transition kinetic pathways

ice | low-density amorphous ice | high-density amorphous ice | amorphization

Ordinary ice displays diverse phase transitions at low temperature and high pressure (1). Phenomena such as pressure-induced amorphization of crystalline ice, amorphous–amorphous transitions, and recrystallization of amorphous ice have become archetypal examples of polymorphism that are relevant to a wide range of topics in materials research (2–7). Many studies have been devoted to understand the origin of these novel transitions. For ice, there are two proposed mechanisms (2, 8–12). One is based on thermodynamic equilibrium theory and the other attributes the transformation to a mechanical instability in the solid state. Recent in situ X-ray diffraction experiments under rapid (de)compression show that the kinetics of the structural transformation is governed by the interplay of the timescales between external (de)compression beyond the equilibrium phase boundary and the intrinsic phase transformation (13–16). In a recent neutron-diffraction experiment, it was reported that ice Ih transforms to ice IX at 100 K instead of amorphizing if the compression process is long enough to meet the time required for thermally driven crystalline–crystalline transition (17). Therefore, one would expect different kinetic behavior or perhaps transformation pathways with respect to the time duration and with temperature (13, 14). A case in point is the “reverse” transformation from the decompression of crystalline ice VII (or VIII). In this respect, fundamental knowledge on kinetically driven pathways, underlying atomistic mechanisms, and the relationship between temperature and time in structural evolution of the metastable high-pressure ices

toward their thermodynamically stable counterparts is rather scarce. Here, we present results of an investigation on the temperature dependence of the kinetic pathway in the conversion of metastable ice VII, recovered at low temperature and low pressure, to the thermodynamically stable ice I.

At low pressure (< 0.2 GPa), crystalline ice I (hexagonal Ih, Ic, and various turbostratic structures) has an open structure with water molecules surrounded tetrahedrally by four others (18–21). In comparison, high-pressure (>2 GPa) dense proton-disordered ice VII phase (or that of its low-temperature proton-ordered analog, ice VIII) consists of two independent interpenetrating H-bonded frameworks (22). Between them, several crystalline forms (e.g., ice II, ice IX, XV, VI, ... etc.) and amorphous forms featuring intermediate densities have been observed (23). Finite-temperature lattice-dynamics calculations have predicted that ice VIII becomes mechanically unstable at low pressures (24). Yet, ice VII/VIII can be recovered at low pressure and low temperature (25, 26). This metastability is due to the large structural disparity with ice I, for which an activation barrier is required to be overcome to realize the substantial structural rearrangements of the myriad of local hydrogen-bond networks. Thus, conversion to the thermodynamically stable

Significance

The kinetics of the structural evolution from crystalline ice (ice VII or ice VIII) toward thermodynamically stable ice I at ambient pressure have been characterized using time-resolved in situ X-ray diffraction. The time resolution captures events that were not observed previously and reveals a complex kinetic pathway with three distinctive transitions, i.e., amorphization, amorphous–amorphous, and crystallization of amorphous ice into ice I. The first two transitions exhibit different thermally activated mechanism above and below 110 K. Molecular-dynamics simulations show the transition involves a large change in density and substantial displacements of water at the nanoscale. This study presents a perspective on the metastability and complexity of the energy landscape in temperature/time-dependent structural evolution in amorphous ices.

Author contributions: C.L., J.S.T., and W.Y. designed research; C.L., X.L., X.Y., J.S.T., J.S.S., B.W., M.L., W.Y., and H.-K.M. performed research; C.L., J.S.T., and N.J.E. analyzed data; and C.L., J.S.T., and N.J.E. wrote the paper.

The authors declare no competing interest.

This article is a PNAS Direct Submission.

Published under the PNAS license.

¹To whom correspondence may be addressed. Email: John.Tse@usask.ca or yangwg@hpstar.ac.cn.

This article contains supporting information online at <https://www.pnas.org/lookup/suppl/doi:10.1073/pnas.2007959117/-DCSupplemental>.

First published June 22, 2020.

form is kinetically inhibited. This interesting observation raises questions regarding kinetic pathways and possible intermediate phases related to the transformation from metastable ice VII/VIII recovered at low pressure to the thermodynamically stable form of ice I under different P - T conditions.

Previous experimental studies have shown that, upon warming at ambient pressure, recovered ice VIII (or ice VII) converts simply to LDA at ~ 120 K and crystallizes into ice I at ~ 150 K (12, 25–28). Later, rapid decompression experiments also support the same sequence of ice VIII \rightarrow LDA \rightarrow ice I at temperatures of 140–165 K (14). However, there is a lack of structural information and kinetic information along these successive transformations. Moreover, the absence of intermediate high-density amorphous (HDA) phase is surprising, as it has a density and local structure similar to crystalline ice VIII (or ice VII) (29). Therefore, if ice VIII recovered at low pressure is mechanically unstable, one would anticipate that the transformation of ice VIII into HDA should be a favorable initial step (24). So, an important question—indeed, one which motivates the present study—is “Can we obtain a new perspective on the interrelationship of polymorphism of ice, and unravel its underpinning complexities from studying ice-transition kinetic pathways?” To investigate this challenging high-level hypothesis, we performed in situ time-resolved X-ray diffraction experiments and molecular-dynamics calculations, starting from ice VII/VIII under different P - T conditions. As will be elaborated on in detail below, the present study provides a perspective on the kinetic effects of structural transformations between the metastable amorphous phases.

Results

We studied the structural evolution of high-pressure ice VII recovered at low pressure and different temperatures using time-resolved synchrotron X-ray diffraction (See *Materials and Methods* for details). The ice VII phase was prepared by compressing the low-pressure phase ice I (ice Ic or Ih) to ≥ 5 GPa at a given temperature between 80 and 155 K. In the compression, ice Ic/Ih transforms to HDA or other high-pressure crystalline phases, and eventually to ice VIII (11). The presence of ice VIII is easily identified from the splitting of the first Bragg peak (*SI Appendix, Fig. S1*). The sample was then decompressed quickly

to vacuum pressure (~ 5 mTorr), while maintaining the temperature. During this process, the split Bragg reflections of ice VIII merged into a single sharp peak, indicating the formation of proton-disordered ice VII (*SI Appendix, Fig. S1*). The formation of ice VII at low temperature has been reported previously (25), but not clearly explained. Note that ice VII is the thermodynamically stable phase at temperatures above 270 K and pressures above 2 GPa. The subtle rearrangement from proton-order to a proton-disorder H-bond network results from elastic relaxation in which the internal energy (pressure-volume work) gained from depressurization of high-pressure ice VIII provides the required activation to promote randomization of the hydrogen atoms upon the release of pressure.

Fig. 1A shows the diffraction patterns for the transformation from ice VII to ice I upon isobaric heating at constant surrounding pressure (~ 5 mTorr in cryostat chamber). At a slow heating rate (< 0.5 K/min), the characteristic Bragg reflections of ice VII start to lose intensities at ~ 86 K (Fig. 1A and *SI Appendix, Fig. S2*). Concomitantly, a “halo” peak appears at $Q = \sim 2.14 \text{ \AA}^{-1}$ (blue arrow), indicating the formation of HDA. The intensity of the first sharp diffraction peak of HDA increases with temperature. From 107 K, another broad peak with $Q = \sim 1.73 \text{ \AA}^{-1}$ starts to emerge, signaling the presence of LDA. Upon further warming, the relative intensity of the LDA phase increases with simultaneous decrease in the intensities of the broad peak at $Q = \sim 2.14 \text{ \AA}^{-1}$, attributed to HDA, and the Bragg reflections of ice VII. At ~ 125 K, only feature redolent of LDA remains. LDA starts to crystallize into ice I with stack faults (i.e., I_{sd}) above 150 K, consistent with previously reported crystallization of LDA (26, 27, 30, 31). Ice I_{sd} transforms to ice Ih when the sample is heated to 210 K (*SI Appendix, Fig. S3*). The crystalline pattern of ice Ih disappears above 230 K due to vaporization in vacuum. The kinetic nature of the transformation processes is confirmed by the measurement of the diffraction patterns at different heating rates (*SI Appendix, Fig. S3*). The isobaric heating experiments reveal the following steps in the structural evolution of metastable ice VII toward thermally stable ice I in vacuum environment: initial transformation of ice VII to HDA, followed by HDA–LDA transition, and then crystallization of LDA into ice I upon heating. This sequence is different

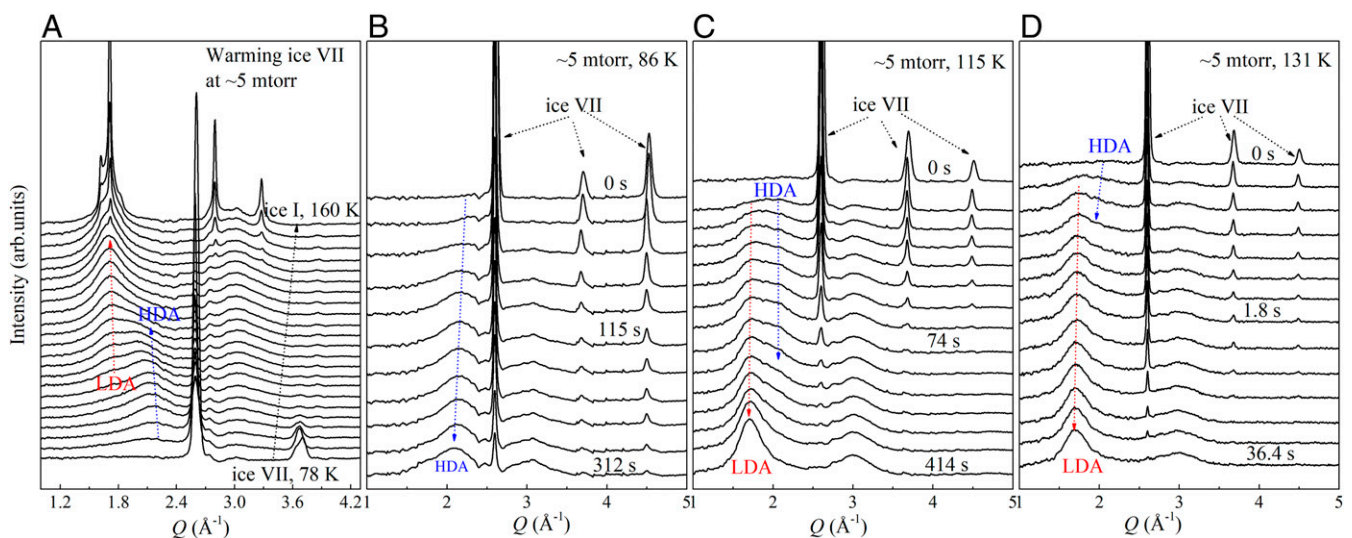


Fig. 1. Structural evolution of metastable ice VII at ~ 5 mTorr and various temperatures. (A) Temperature-dependent structural evolution from metastable ice VII recovered at ~ 5 mTorr to crystalline ice I upon warming from 78 to 160 K at a heating rate of < 0.5 K/min. After rapid decompression, the sample was heated immediately. Blue arrows indicate a broad peak of HDA at $Q = \sim 2.13 \text{ \AA}^{-1}$; the broad peak at $Q = \sim 1.73 \text{ \AA}^{-1}$, indicated by the red arrow, originates from LDA. (B, C, and D) depict the time-dependent structural evolution of ice VII at ~ 5 mTorr and temperatures of 86, 115, and 131 K.

from previous reports, in which HDA was not observed (12, 14, 25–28).

To probe the timescale and thermal effect on each step, we focus on the structural evolution of ice VII at constant P - T conditions (Fig. 1 *B–D* and *SI Appendix*, Figs. S4–S6). At all temperature, ice VII starts to amorphize once it is formed from ice VIII by rapid decompression from ~ 5 GPa to ~ 5 mTorr. At 86 K, ice VII relaxes gradually to HDA (Fig. 1*B*). Under this conditions, ice VII can be still observed to coexist with HDA up to 312 s. At this temperature, the HDA \rightarrow LDA transition is not observed within the duration of the experiment. This observation indicates clearly that the transformation is kinetically hindered at low temperature. At 110 and 115 K, ice VII first transforms to HDA, followed by the HDA-to-LDA transition (Fig. 1*C* and *SI Appendix*, Fig. S4). At higher temperatures (127, 131, and 140 K), the weak halo at $Q = \sim 2.1 \text{ \AA}^{-1}$, attributed to HDA, is still observable together with LDA; but, the HDA phase formed from ice VII has only a very short survival time (duration of existence), less than 100 ms, before transforming rapidly to LDA (Fig. 1*D* and *SI Appendix*, Fig. S5). The LDA phase crystallizes to ice I above 140 K within at least half an hour (14). It is noted that the HDA phase is not observed above 150 K (*SI Appendix*, Fig. S6), as the timescale for the HDA–LDA transition is very short and beyond the time resolution of the detection capability.

Fig. 2 compares the plots of the logarithm of the “duration time” (τ) as a function of temperature for ice VII \rightarrow HDA (amorphization), HDA–LDA transition, and the crystallization of LDA. The duration time for the amorphization process is defined as the time required for the conversion from the precursor to the product by 50% (*SI Appendix*, Fig. S7). The τ - T data are then fitted to the Arrhenius equation $\tau = \tau_0 \exp(Q/RT)$ for kinetic process (32–34), where τ_0 is a constant characteristic time, Q is the activation energy associated with the process, and R is the universal gas constant. It is clear from Fig. 2 that in the temperature range of 85–155 K the amorphization process displays two different Arrhenius behaviors with a discontinuity at around 110 K. Below 110 K, the duration time for amorphization is almost independent of temperature with an approximately constant transformation rate ($1/\tau$). The fit yields an activation

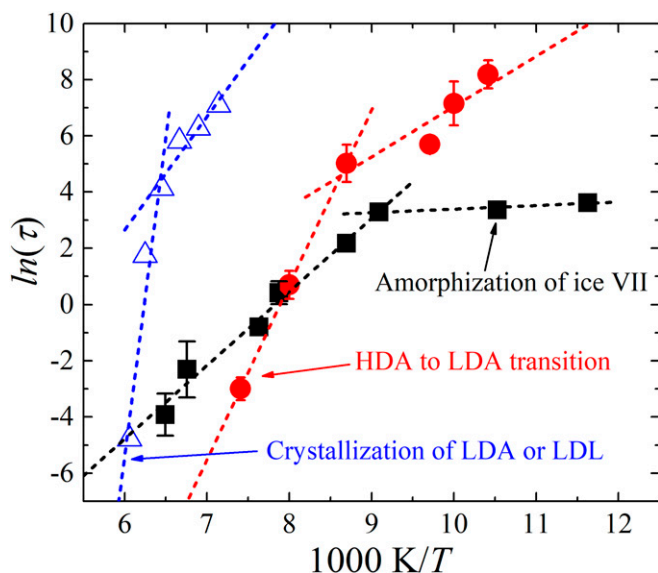


Fig. 2. Temperature dependence of the duration time (τ , in seconds) for amorphization of ice VII, HDA–LDA transition, and crystallization of LDA. Duration time for HDA–LDA transition is partially obtained by rapid decompression of HDA from high pressure to ~ 5 mTorr and monitoring the relaxation of HDA. The data for the crystallization of LDA are from ref. 14.

energy of 1.1(2) kJ/mol and τ_0 of 8(3) s. The small activation energy and almost temperature-independent τ implies that the amorphization of ice VII at ~ 5 mTorr below 110 K is driven by a mechanical instability which requires negligible thermal energy, but the atomic displacements associated with the structural change is very slow. In comparison, above 110 K, the logarithm of τ for the amorphization of ice VII correlates linearly with inverse of the temperature. τ decreases drastically from ~ 27 s at 110 K to below 20 ms at 154 K. Fitting the 110 K τ - T data yields an activation energy of 22(1) kJ/mol and τ_0 of $7(1) \times 10^{-10}$ s. Now, the structural transformation, still due to mechanical instability, occurs in a faster time frame assisted by thermal activation. The temperature plays a more and more important role in the amorphization of ice VII above 110 K as the thermal energy promotes the kinetically controlled amorphization. Interestingly, we note that the background thermal energy, RT , is of the order of 1 kJ/mol at this “cross-over” temperature for kinetic-transition regime; in addition to the depressurization-induced pressure-volume work of expansion from ice VII to HDA, this bears the “signature” of the configurational-energy difference between ice VII and HDA (somewhat higher than 1 kJ/mol, on a per-molecule basis)—owing to ice-VII-lattice mechanical instability (*vide infra*). With thermal activation at ~ 110 K supplying the additional energy required to overcome this mechanical-instability-driven density change, and (loss of interpenetrating) hydrogen-bonding-network relaxations to a lower-energy structure, it is unsurprising to witness this VII–HDA kinetic cross-over temperature at ~ 110 K, i.e., with substantial acceleration of the amorphization above 110 K, as it now becomes a thermally controlled process (with the RT thermal-energy term now dominating).

The time duration for the HDA \rightarrow LDA transition is defined as the persistence time of HDA, the time between the first detection and disappearance of HDA observed at ~ 5 mTorr in the experiments. As expected, this duration time decreases with increasing temperature, since the transition involves, yet again, a density change of $>20\%$ and the substantial rearrangement of the H-bond networks. Incidentally, even though the definition of the duration time is different from the amorphization of ice VII, a discontinuity is also observed at ~ 115 K from the Arrhenius fits (Fig. 2). Below 115 K, the Arrhenius fit of the τ - T data yields an activation energy of 15(2) kJ/mol and τ_0 of 1.9×10^{-5} s. Above 115 K, the corresponding values are $Q = 51(1)$ kJ/mol and $\tau_0 = 4.8(1) \times 10^{-23}$ s. It is surprising that both amorphization of ice VII and HDA \rightarrow LDA transition show a discontinuity in the temperature-dependent duration times at around 110–115 K. In both cases, the transition timescale is very short above this temperature. The transition processes show a strong temperature dependence, indicating that the thermal energy is sufficient to overcome the energy barriers and the kinetics is thermally activated. Below the discontinuities, the transitions are assisted only by stochastic thermal excitations and the duration times are much longer. Incidentally, changes in the Arrhenius behavior of the structural transition process are close to the previously reported glass-transition temperature of HDA that has been explained as the cross-over from nondiffusive motion to nanoscale diffusion in amorphous ice (35–37). It should be noted that the activation energy for both ice VII amorphization and HDA \rightarrow LDA transitions at low temperature are smaller than that above the discontinuity. This observation indicates there are two distinctive mechanistic paths for the transition below and above the discontinuity. This is related to that both HDA and LDA have multienergy minima in the amorphous state (27, 38–40). Two different transformation paths can be explained as follows. Below the discontinuity temperature, the system has low thermal energy and the amorphization of ice VII is driven by the mechanical instability of the crystal lattice [i.e., violating Born’s stability condition, as suggested by an earlier calculation (8, 10,

41)], and the structural transformation is spontaneous, requiring little activation energy. The HDA formed is not annealed and relaxes continuously with time toward more stable local minima. At high temperature, although the mechanism is still due to a lattice instability, the system now acquires sufficient thermal energy to overcome the multiple energy barriers. Therefore, ice VII transforms directly to the more relaxed amorphous state. We believe the discontinuities in the amorphization and HDA → LDA transformations are not accidental and may share the same origin. The discontinuity in HDA → LDA transformation is remarkably close to the glass-transition temperature observed in HDA (35–37). It is likely these two phenomena are related. Above the glass-transition temperature, the thermal energy enhances the mobility of atoms and so its duration shortens. Furthermore, the HDA from ice VII should also experience the same effects as HDA formed from ice VII will transform to LDA concurrently. The depletion of HDA accelerates the rate of ice VIII → HDA transformation.

To further investigate underlying atomistic mechanisms, molecular-dynamics (MD) calculations at isobaric heating and isothermal decompression were performed [see details in *Materials and Methods* and previous studies (42–45)]. Fig. 3 summarizes the results of simulations on the decompression of ice VIII at several selected temperatures. Fig. 3A and B show that, below 120 K and 0.2 GPa, ice VIII persists even down to zero pressure, indicating the metastability and therefore, it can be quenched, as revealed by experiment. Above 130 K, ice VIII collapses rapidly from $\sim 1.49 \text{ gm/cm}^3$ to about 1.06 gm/cm^3 when the pressure is released from 1 to 0.3 kbar within the timescale of the simulation ($\sim 1 \text{ ns}$). The density of the ice structure is intermediate between extended HDA and LDA (0.94 gm/cm^3) recovered at ambient pressure. We were able to capture the detailed atomistic process for the successive ice VIII → HDA → LDA transformations

from a long MD simulation (3 ns) at 130 K. The results provide a pictorial and atomistic description on the gradual transformation from ice VIII to a low-density ice (1.0 gm/cm^3) upon the release of pressure. The calculation shows, starting at 1.3 gm/cm^3 at 1 kbar, that the density of the model drops to 1.2 gm/cm^3 at 0.6 kbar, and then to 1.08 gm/cm^3 at 0.2 kbar. Additional calculations were performed by holding the pressure at 0.2 kbar and 130 K (Fig. 3C). Fig. 3C shows continuous lowering of the density from 1.10 to 1.08 gm/cm^3 within a time segment of 300 ps. It is not unreasonable to anticipate that, upon prolonged simulation time, the density of the model may reach that of LDA at $\sim 0.94 \text{ gm/cm}^3$.

The structural arrangement for the HDA to LDA transformation can be analyzed from calculations of the probability of the nonhydrogen bonded [pnhb(r)] second-nearest neighbor, which serves as an indicator of the presence of an interpenetrating H-bond network (43). The intrusion of a “fifth” oxygen atom at the first coordination shell is the “fingerprint” of HDA (46, 47). This is as a result of the onset of formation of interpenetrating H-bond networks in the structure. In dense crystalline ices, the local coordination of the water molecules (oxygen atoms) remains tetrahedral under very high pressure. Pressure densification can only be achieved by the formation of interpenetrating H-bond networks. To this end, the 0.3-ns MD trajectory at 130 K is divided into three equal time segments (Fig. 3D). In the initial period (part 1), the ice VIII is intact. Since ice VIII is composed of two proton-ordered and interpenetrating H-bonded networks, the pnhb(r) is very high. The probability is reduced substantially in the second and third period (part 2 and 3), indicating the partial destruction of the interpenetrating H-bond networks into a single H-bonded network in a low-density ice. This is the exact reverse of the process in the formation interpenetrating H-bonded structure when ice Ih is compressed.

Note that the difference in the experimental densities of recovered HDA (1.27 g/cm^3) and LDA (0.94 g/cm^3) ice, i.e., -0.33 g/cm^3 , is rather substantial. This corresponds to a volume increase of almost 30%, and $\sim 11\%$ increase in the linear dimension ($\sim \sqrt[3]{1.3}$) in LDA. The expansion is due to the relaxation of the second-nearest O-O coordination shell. Since the experimental second-nearest O-O distance in HDA is in the range of 3.5–4.5 Å, the second-nearest-neighboring oxygen atoms will be displaced by 4–5 Å. This order-of-magnitude estimation is supported by examination of the instantaneous oxygen-atom positions from the MD trajectory and is plotted for two randomly selected water molecules within 1 ns during the decompression of ice VIII at 130 K (*SI Appendix, Fig. S8*). Initially, the water molecules oscillate around their respective mean positions of ice VIII (indicated by the almost spherical distribution). When the ice VIII structure is converted to HDA, there is a sudden displacement of the water atoms as indicated by the large movement of the atom positions. With the passage of time, the structure transforms gradually to a lower-density form, and, evidently, the spatial “spread” of the water-molecule positions becomes larger, as the water is seeking equilibrium positions in the voids formed by the expansion in volume. From the size of the simulation model, one can visualize the disordering of the water in the lower-density structure (*SI Appendix, Fig. S8*). One can estimate the size of the atom displacement to be about 10% of the cell length or around 5 Å. This estimate displacement is in reasonable agreement with recent experimental measurement showing atom displacements on the order of nanometer scale (36). At this stage, since the transformation is associated with the relaxation of the local water environment, the water molecules are categorically not undergoing diffusive motion, as their movements are not continuous, but are rather confined within a localized region of space, and are driven mechanically by bulk-volume expansion.

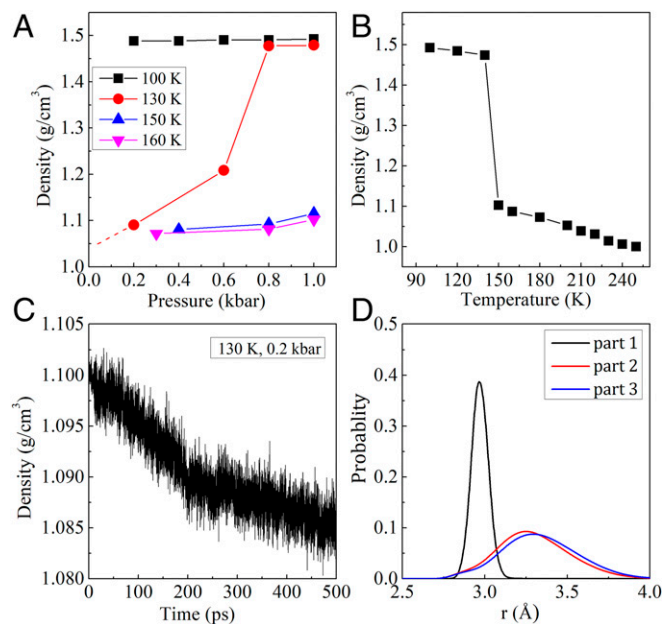


Fig. 3. Changes of densities in the structural evolution of depressurized ice VIII at various temperatures by MD simulation. Change of density as a function of (A) pressure and (B) temperature. (C) Density evolution within a time segment of 500 ps accompanying the structural relaxation at 130 K and 0.2 GPa. (D) Evolution of the pnhb(r) second-nearest neighbor for the simulated ice structure at 130 K and 0.2 GPa. The 0.3-ns trajectory is divided into three time segments (parts 1 to 3). The original distribution of ice VIII is very sharp, indicating the H-bond networks are interpenetrating. The following two segments show significant broadening, indicating the transition to noninterpenetrating networks.

Discussion

In summary, we studied the kinetic process in the structural evolution of ice VII toward ice I at selected P - T conditions. The following three-step process was observed: collapse of ice VII into HDA, HDA–LDA transition, and thermally driven crystallization of LDA into ice I. The sequence mirrors that of pressure-induced amorphization of ice Ih, in which the initial transformation step is driven by mechanical instability and, therefore, kinetically controlled (24). The timescale for each step shows a strong temperature dependence. To quantify the structural evolution from metastable ice VII to ice I, the relative amount of ice VII, HDA, LDA, and ice I as a function of time at various temperatures are estimated according to the kinetic Johnson–Mehl–Avrami–Kolmogorov kinetic model (48–50) from the duration time of each species (Fig. 4), assuming the transformations are homogeneous process. At 90 K, conversion of ice VII to HDA is almost completed within the duration of the experiment. The HDA fraction decreases significantly when the temperature is raised. Small amount of HDA, indicated by a weak halo peak at $Q = \sim 2.1 \text{ \AA}^{-1}$, still can be observed between 120 and 140 K, but the transformation to LDA occurs almost simultaneously. This observation is in agreement with X-ray diffraction results (Fig. 1 and *SI Appendix*, Fig. S5). No HDA was observed at temperature of $>150 \text{ K}$ due to the short transition timescale beyond the experimental resolution (*SI Appendix*, Fig. S6). Compared with HDA, the LDA phase is more stable with large duration timescale. Above 150 K, the maximum fraction of LDA decreases quickly with drastic decrease in the duration time of LDA (Figs. 2 and 4). At 165 K, it is around 20%. The LDA phase is difficult to probe directly in the experiments. For example, the LDA phase cannot be observed directly in the in situ X-ray diffraction patterns in the phase transition from ice VII to ice I at 165 K and 5 mTorr (*SI Appendix*, Fig. S9). Ice I grows together with gradual disappearance of ice VII, but is not synchronous. The intensities of the diffraction peaks of ice I still increase with time after ice VII disappears completely, indicating the existence of LDA. Above 166 K, the maximum fraction of LDA is approximately zero. However, we should not rule out the possibility that the amorphous phase forms first from ice VII and then transforms immediately to ice I, as the amorphization of ice VII is controlled by thermal

effects (especially above the kinetic cross-over temperature of $\sim 110 \text{ K}$).

Materials and Methods

Sample Preparation. The experimental details have been described in previous studies (11, 13, 14). Briefly, the diamond-anvil cells (DACs) with 400–500- μm culets were used for high-pressure and low-temperature experiments in a cryostat. The steel gasket was preindented to a thickness of ~ 80 – $100 \mu\text{m}$. The indented gasket was drilled by laser for a sample hole with a diameter of $\sim 150 \mu\text{m}$. The distilled deionized water was loaded into the sample chamber, together with two ruby spheres located at the center and near the edge of the sample hole. The pressure was determined by the ruby fluorescence method (51).

High-Pressure X-Ray Diffraction Measurements. High-pressure and low-temperature experiments were performed at beamline 16-ID-B at the Advanced Photon Source (APS), Argonne National Laboratory (52) and at beamline BL10XU of Spring-8 (53). Loaded DAC was placed in a cryostat with the sample temperature monitored by the silicon diode sensor. Before cooling, the gas pressure of the cryostat assembly was vacuum-pumped to $<5 \text{ mTorr}$. The entire DAC assembly was then cooled using liquid nitrogen or by a low-vibration closed-cycle helium refrigerator. A heater mounted on the holder allows precise control of DAC temperature. The sample temperature was stable within $\pm 0.5 \text{ K}$ during the experiments. Gas membranes were used to control compression and decompression pathways (54).

In angle-dispersive X-ray diffraction experiments, X-ray with a wavelength of 0.4137 \AA or 0.40663 \AA were focused into a $5 \times 6\text{-}\mu\text{m}^2$ (full width at half maximum) spot on the sample. Two-dimensional diffraction images were collected continuously throughout the compression and decompression process with a PILATUS 1M-F detector at beamline 16-ID-B, APS and a Rigaku R-axis IV++ area detector at BL10XU of Spring-8. The typical exposure time was from 30 to 7 ms, depending on decompression rate and temperature. Diffraction data were analyzed and integrated using the software Dioplas (55). In data analysis, we used a diffraction image of high-pressure crystalline ice VIII as background to obtain a clear diffraction pattern.

MD Simulation. The calculations were conducted at isobaric heating and isothermal decompression [see details in previous studies (42, 43)]. The initial model comprised 3,888 molecules in a tetragonal cell with dimension of $49 \times 48 \times 48 \text{ \AA}^3$. MD calculations were performed with Daresbury Laboratory Polyatomic (DL-POLY) with the 4-site transferrable intermolecular potential (TIP4P/ice) (44, 45). Most MD trajectories were 0.1 ns with an integration time of 1 fs.

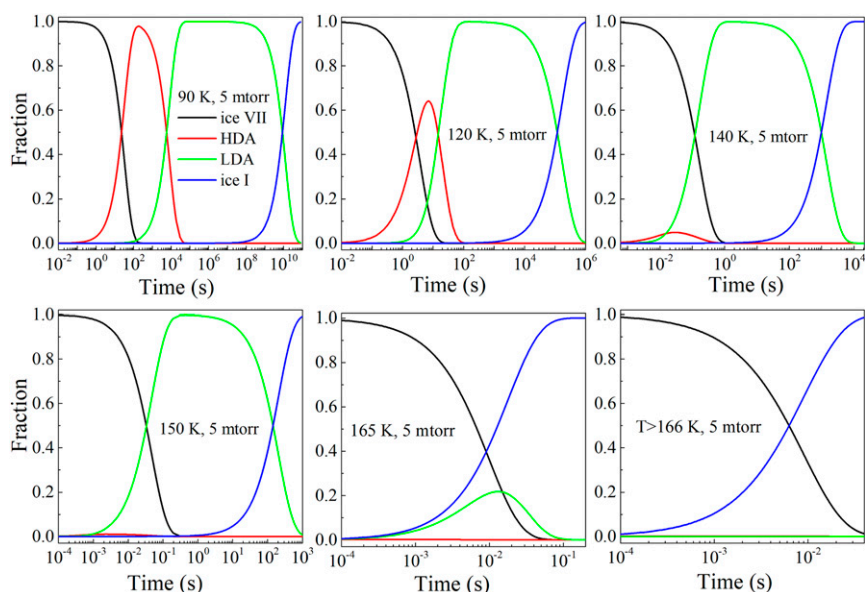


Fig. 4. Calculated fraction of ice VII, HDA, LDA, and ice I as a function of time at various temperatures. It depicts the kinetic process from ice VII to ice I.

Data Availability. The authors declare that all relevant data supporting this study are available within the paper and *SI Appendix*.

ACKNOWLEDGMENTS. The authors thank Saori Kawaguchi, Curtis Kenney-Benson, and Richard Ferry for technical support and acknowledge the financial support from National Nature Science Foundation of China (Grant 11974033, 51527801, and U1930401). In situ high-pressure/low-temperature X-ray diffraction measurements were conducted at sector 16 ID-B, High

Pressure Collaborative Access Team (HPCAT) of APS and at beamline BL10XU of Spring-8. HPCAT operations are supported by the Department of Energy (DOE)–National Nuclear Security Administration (NNSA) under Award DE-NA0001974, with partial instrumentation funding by NSF. APS is a user facility operated for the DOE Office of Science under Contract DE-AC02-06CH11357 by UChicago Argonne, LLC. The synchrotron radiation experiments were performed under the approval of the Japan Synchrotron Radiation Research Institute (Proposals 2019B1059, 2019B4267, and 2019A4273).

1. T. Bartels-Rausch *et al.*, Ice structures, patterns, and processes: A view across the icefields. *Rev. Mod. Phys.* **84**, 885–944 (2012).
2. O. Mishima, L. D. Calvert, E. Whalley, “Melting ice” I at 77 K and 10 kbar: A new method of making amorphous solids. *Nature* **310**, 393–395 (1984).
3. O. Mishima, L. D. Calvert, E. Whalley, An apparently first-order transition between two amorphous phases of ice induced by pressure. *Nature* **314**, 76–78 (1985).
4. K. Amann-Winkel *et al.*, Colloquium: Water’s controversial glass transitions. *Rev. Mod. Phys.* **88**, 11002 (2016).
5. P. Gallo *et al.*, Water: A tale of two liquids. *Chem. Rev.* **116**, 7463–7500 (2016).
6. P. H. Handle, T. Loerting, F. Sciortino, Supercooled and glassy water: Metastable liquid(s), amorphous solid(s), and a no-man’s land. *Proc. Natl. Acad. Sci. U.S.A.* **114**, 13336–13344 (2017).
7. P. G. Debenedetti, Supercooled and glassy water. *J. Phys. Condens. Matter* **15**, R1669–R1726 (2003).
8. J. S. Tse, Mechanical instability in ice Ih. A mechanism for pressure-induced amorphization. *J. Chem. Phys.* **96**, 5482–5487 (1992).
9. O. Mishima, Relationship between melting and amorphization of ice. *Nature* **384**, 546–549 (1996).
10. J. S. Tse *et al.*, The mechanisms for pressure-induced amorphization of ice Ih. *Nature* **400**, 647–649 (1999).
11. C. Lin *et al.*, Kinetically controlled two-step amorphization and amorphous-amorphous transition in ice. *Phys. Rev. Lett.* **119**, 135701 (2017).
12. Y. Wang, H. Zhang, X. Yang, S. Jiang, A. F. Goncharov, Kinetic boundaries and phase transformations of ice i at high pressure. *J. Chem. Phys.* **148**, 44508 (2018).
13. C. Lin, J. S. Smith, X. Liu, J. S. Tse, W. Yang, Venture into water’s no man’s land: Structural transformations of solid H₂O under rapid compression and decompression. *Phys. Rev. Lett.* **121**, 225703 (2018).
14. C. Lin, J. S. Smith, S. V. Sinogeikin, G. Shen, Experimental evidence of low-density liquid water upon rapid decompression. *Proc. Natl. Acad. Sci. U.S.A.* **115**, 2010–2015 (2018).
15. M. Bauer, M. Elsaesser, K. Winkel, E. Mayer, T. Loerting, Compression-rate dependence of the phase transition from hexagonal ice to ice II and/or ice III. *Phys. Rev. B* **77**, 220105(R) (2008).
16. J. Y. Chen, C. S. Yoo, High density amorphous ice at room temperature. *Proc. Natl. Acad. Sci. U.S.A.* **108**, 7685–7688 (2011).
17. C. A. Tulk, J. J. Molaison, A. R. Makhluf, C. E. Manning, D. D. Klug, Absence of amorphous forms when ice is compressed at low temperature. *Nature* **569**, 542–545 (2019).
18. T. L. Malkin, B. J. Murray, A. V. Brukhno, J. Anwar, C. G. Salzmann, Structure of ice crystallized from supercooled water. *Proc. Natl. Acad. Sci. U.S.A.* **109**, 1041–1045 (2012).
19. W. F. Kuhs, C. Sippel, A. Falenty, T. C. Hansen, Extent and relevance of stacking disorder in “ice I(c)”. *Proc. Natl. Acad. Sci. U.S.A.* **109**, 21259–21264 (2012).
20. T. L. Malkin *et al.*, Stacking disorder in ice I. *Phys. Chem. Chem. Phys.* **17**, 60–76 (2015).
21. A. Goto, T. Hondoh, S. Mae, The electron density distribution in ice Ih determined by single-crystal x-ray diffractometry. *J. Chem. Phys.* **93**, 1412–1417 (1990).
22. R. J. Nelmes *et al.*, Neutron diffraction study of the structure of deuterated ice VIII to 10 GPa. *Phys. Rev. Lett.* **71**, 1192–1195 (1993).
23. E. Sanz, C. Vega, J. L. Abascal, L. G. MacDowell, Phase diagram of water from computer simulation. *Phys. Rev. Lett.* **92**, 255701 (2004).
24. J. S. Tse, V. P. Shpakov, V. R. Belosludov, Vibrational spectrum, elastic moduli and mechanical stability in ice VIII. *J. Chem. Phys.* **111**, 11111–11116 (1999).
25. S. Klotz *et al.*, Metastable ice VII at low temperature and ambient pressure. *Nature* **398**, 681–684 (1999).
26. D. D. Klug, Y. P. Handa, J. S. Tse, E. Whalley, Transformation of ice VIII to amorphous ice by “melting” at low temperature. *J. Chem. Phys.* **90**, 2390–2392 (1989).
27. J. J. Shephard, S. Klotz, M. Vickers, C. G. Salzmann, A new structural relaxation pathway of low-density amorphous ice. *J. Chem. Phys.* **144**, 204502 (2016).
28. Y. Yoshimura, H. K. Mao, R. J. Hemley, Direct transformation of ice VII’ to low-density amorphous ice. *Chem. Phys. Lett.* **420**, 503–506 (2006).
29. S. Klotz *et al.*, Structure of high-density amorphous ice under pressure. *Phys. Rev. Lett.* **89**, 285502 (2002).
30. W. Hage, A. Hallbrucker, E. Mayer, G. P. Johari, Crystallization kinetics of water below 150 K. *J. Chem. Phys.* **100**, 2743–2747 (1994).
31. W. Hage, A. Hallbrucker, E. Mayer, G. P. Johari, Kinetics of crystallizing D₂O water near 150 K by Fourier transform infrared spectroscopy and a comparison with the corresponding calorimetric studies on H₂O water. *J. Chem. Phys.* **103**, 545–550 (1995).
32. A. K. Singh, The kinetics of some pressure-induced transformations. *Mater. Sci. Forum* **3**, 291–306 (1985).
33. N. V. Chandra-Shekar, K. G. Rajan, Kinetics of pressure induced structural phase transitions—A review. *Bull. Mater. Sci.* **24**, 1–21 (2001).
34. S. Glasstone, K. J. Laidler, H. Eyring, *Theory of Rate Processes*, (McGraw-Hill, New York, 1941).
35. C. R. Hill *et al.*, Neutron scattering analysis of water’s glass transition and micropore collapse in amorphous solid water. *Phys. Rev. Lett.* **116**, 215501 (2016).
36. F. Perakis *et al.*, Diffusive dynamics during the high-to-low density transition in amorphous ice. *Proc. Natl. Acad. Sci. U.S.A.* **114**, 8193–8198 (2017).
37. K. Amann-Winkel *et al.*, Water’s second glass transition. *Proc. Natl. Acad. Sci. U.S.A.* **110**, 17720–17725 (2013).
38. K. Winkel, D. T. Bowron, T. Loerting, E. Mayer, J. L. Finney, Relaxation effects in low density amorphous ice: Two distinct structural states observed by neutron diffraction. *J. Chem. Phys.* **130**, 204502 (2009).
39. R. J. Nelmes *et al.*, Annealed high-density amorphous ice under pressure. *Nat. Phys.* **2**, 414–418 (2006).
40. T. Loerting, C. Salzmann, I. Kohl, E. Mayer, A. A. Hallbrucker, Second distinct structural “state” of high-density amorphous ice at 77 K and 1 bar. *Phys. Chem. Chem. Phys.* **3**, 5355–5357 (2001).
41. T. Strassel, A. M. Saitta, S. Klotz, M. Braden, Phonon dispersion of ice under pressure. *Phys. Rev. Lett.* **93**, 225901 (2004).
42. M. P. Allen, D. J. Tildesley, *Computer Simulation of Liquid*, (Oxford University Press, ed. 2, 2017).
43. X. Yong, J. S. Tse, N. J. English, optPBE-vdW density functional theory study of liquid water. *Can. J. Chem.* **95**, 1205–1211 (2017).
44. I. T. Todorov, W. Smith, K. Trachenko, M. T. Dove, DL_POLY_3: New dimensions in molecular dynamics simulations via massive parallelism. *J. Mater. Chem.* **16**, 1911–1918 (2006).
45. J. L. F. Abascal, E. Sanz, R. García Fernández, C. Vega, A potential model for the study of ices and amorphous water: TIP4P/ice. *J. Chem. Phys.* **122**, 234511 (2005).
46. J. S. Tse, Pressure induced amorphization of ice Ih. *J. Chem. Phys.* **92**, 3992–3994 (1990).
47. J. L. Finney *et al.*, Structure of a new dense amorphous ice. *Phys. Rev. Lett.* **89**, 205503 (2002).
48. J. W. Christian, *The Theory of Transformation in Metals and Alloys*, (Pergamon, Oxford, 2002).
49. M. Avrami, Kinetics of phase change. I general theory. *J. Chem. Phys.* **7**, 1103–1112 (1939).
50. M. Avrami, Kinetics of phase change. II transformation-time relations for random distribution of nuclei. *J. Chem. Phys.* **8**, 212–224 (1940).
51. H. K. Mao, J. Xu, P. M. Bell, Calibration of the ruby pressure gauge to 800 kbar under quasi-hydrostatic conditions. *J. Geophys. Res.* **91**, 4673–4676 (1986).
52. J. S. Smith *et al.*, Developments in time-resolved high pressure x-ray diffraction using rapid compression and decompression. *Rev. Sci. Instrum.* **86**, 72208 (2015).
53. N. Hirao *et al.*, New developments in high-pressure x-ray diffraction beamline for diamond anvil cell at Spring-8. *Mater. Radiat. Extremes* **5**, 18403 (2020).
54. S. V. Sinogeikin *et al.*, Online remote control systems for static and dynamic compression and decompression using diamond anvil cells. *Rev. Sci. Instrum.* **86**, 72209 (2015).
55. C. Prescher, V. P. Prakapenka, DIOPTAS: A program for reduction of two-dimensional X-ray diffraction data and data exploration. *High Press. Res.* **35**, 223–230 (2015).